

Magnetic field tomography

Ph.W. Courteille^{1,a}, S.R. Muniz¹, K. Magalhães¹, R. Kaiser², L.G. Marcassa¹, and V.S. Bagnato¹¹ Instituto de Física de São Carlos, USP, Caixa Postal 369, CEP 13560-970, São Carlos/SP, Brazil² Laboratoire Ondes et Désordre^b, 1361 route des Lucioles, 06560 Valbonne, France

Received 20 March 2001 and Received in final form 12 May 2001

Abstract. Neutral atoms may be trapped *via* the interaction of their magnetic dipole moment with magnetic field gradients. One of the possible schemes is the cloverleaf trap. It is often desirable to have at hand a fast and precise technique for measuring the magnetic field distribution. We use for instantaneous imaging the equipotential lines of the magnetic field a diagnostic tool which is based on spatially resolved observation of the fluorescence emitted by a hot beam of sodium atoms crossing a thin slice of resonant laser light within the magnetic field region to be investigated. The inhomogeneous magnetic field spatially modulates the resonance condition between the Zeeman-shifted hyperfine sublevels and the laser light and therefore the amount of scattered photons. We apply this technique for mapping the field of our cloverleaf trap in three dimensions under various conditions.

PACS. 32.60.+i Zeeman and Stark effects – 07.55.Ge Magnetometers for magnetic field measurements

1 Introduction

For two decades, the invention of cooling and trapping techniques for neutral atoms boosts the field of cold atomic physics and several years ago even led to the realization of the long expected goal of *Bose-Einstein condensation* (BEC) in dilute atomic gases, followed by a wealth of remarkable experiments on atom lasing and superfluidity of condensed gases. Most trapping configurations are based on light forces or magnetic field gradients or combinations of both. The most frequently used trap for neutral atom trapping is the *Magneto-Optical Trap* (MOT) [1]. MOTs have allowed the confinement of more than 10^{10} atoms [2] at temperatures well below 100 μ K and densities up to 10^{12} cm^{-3} . Radiation trapping by the optically thick cloud, however, sets a limit to further compression due to photon rescattering [3]. Even employing more sophisticated schemes [4], the highest phase space density achieved today remains at about one order of magnitude below the threshold to Bose-Einstein condensation. The phenomenon of radiation trapping is intrinsically connected to the fact that in magneto-optical traps the restoring force comes from the radiation pressure exerted by the laser beams. Alternative trapping schemes based on the dipole force of far-detuned laser beams avoid the radiation trapping problem [5,6]. A different approach is to exploit the weak interaction of the dipole moment of paramagnetic atoms with magnetic field gradients. Magnetic fields can be designed to generate local minima in

free space capable of acting as trapping potentials. Several types of magnetic traps have been successfully used in BEC experiments like the *Time-Orbiting Potential* (TOP) trap [7] and various *Ioffe-Pritchard* (IP) type traps [8,9]. Because magnetic traps are generally weak, large magnetic fields and loading with precooled atoms is required. Generally the atoms are precooled in a standard MOT and then transferred into the magnetic trap. In the absence of laser light the magnetic trap requires a new kind of cooling mechanism. The only mechanism that has successfully led to BEC up to now is *Forced Radiofrequency Evaporation* [10,11]. A necessary condition for evaporation to work is that the rate of elastic collisions between the trapped atoms be large enough to maintain the cloud in thermal equilibrium during the evaporation process which must take place within a period shorter than the trap lifetime [12]. Large collision rates mean big atomic clouds and/or steep trapping potentials.

This work is motivated by our need to characterize our *cloverleaf trap* which is, in principle, a Ioffe-Pritchard type trap [13]. The necessity of optimizing the efficiency for loading, trapping and evaporative cooling sets tight conditions for the design of the magnetic coils and the current supplying circuitry. *E.g.*, the field gradient must be rather strong and capable of being varied over a wide range. It is important to calibrate the secular frequencies, which essentially govern the shape of the trapped atomic cloud, as a function of the control parameters. Therefore we need a precise control of the fields and a suitable way of measuring and monitoring them. Measuring magnetic fields is usually performed with Hall probes. However, very often the region of space to be analyzed is within a vacuum

^a e-mail: Philippe.Courteille@up.univ-mrs.fr^b FRE 2302 CNRS

recipient and thus not accessible to massive probes. We use the idea of fluorescence imaging magnetic fields [14] to develop a simple technique for the instantaneous mapping of magnetic field equipotential lines in two dimensions within a closed vacuum recipient. This technique that we call *Magnetic Field Tomography* (MFT) can even be extended to allow a three-dimensional reconstruction of the complete magnetic vector field. The method provides a simple and reliable diagnostic tool for quantifying the field distribution of our magnetic trap for any set of values of the control parameters.

This paper is organized as follows. In Section 2, we present our magnetic trapping experiment and briefly expose our approach to calculating the magnetic field distribution. In Section 3, we introduce our Magnetic Field Tomography technique. We tested the technique and present experimental results in Section 4, where we also show how to process the experimental data and compare the results to the calculated fields. We conclude our paper with a general discussion.

2 The magnetic trap

Magnetic traps are usually built with current carrying coils or permanent magnets [15]. In the first case, high magnetic field gradients generally require high currents flowing through the coils. In special cases, high gradients may be achieved with lower currents [16,17]. The main constraints for the design of the coils for the cloverleaf trap arise from the geometry of the vacuum chamber and by the power supply available: in our setup, the minimum distance between the coils and the center of the trap is 15 mm. We apply up to 300 A and need to dissipate the 10 kW resistive heat by cooling the coils with a high-pressure water flow passing through the hollow wires. Our magnetic cloverleaf trap is schematically shown in Figure 1. Radial confinement of the atoms is assured by four pairs of coils in anti-Helmholtz configuration (off-center coils in Fig. 1) producing a quadrupolar waveguide field along the symmetry axis. Axial confinement is realized *via* a magnetic bottle (inner and outer axially centered coils in Fig. 1). The (inner) pinch coils create the necessary field curvature, and a pair of (outer) antibias coils in Helmholtz configuration compensates the large central offset produced by the pinch coils to a variable amount. As said earlier, to initiate run-away evaporative cooling, we must be able to realize large interatomic elastic collision rates. This is achieved by compressing the magnetic trap: at the time of loading the trap from the MOT the mean secular frequency is typically $\omega_{\text{trap}} \approx 2\pi \times 20$ Hz (the transfer efficiency is best when the curvatures of the MOT and the magnetic trap are approximately matched), and the secular frequency of the fully compressed trap is $\omega_{\text{trap}} \approx 2\pi \times 200$ Hz. In the case of the cloverleaf trap, the compression is controlled *via* the antibias field.

Precise control of the magnetic field bias is also important because it fixes an offset for the resonant radiofrequency used for evaporative cooling: the evaporating surface [18] is set by the condition that the radiofrequency

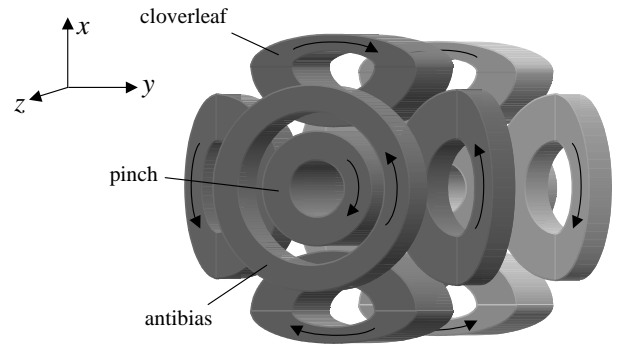


Fig. 1. Scheme of the cloverleaf trap. The cloverleaf coils (blue) produce a radially linear magnetic field. The pinch coils (red) produce an axially confining magnetic bottle. The antibias coils (green) are Helmholtz coils and serve to compensate the magnetic field offset.

balances the shift of the atomic energy levels induced by the local magnetic field $\hbar\omega_{\text{rf}} = |\boldsymbol{\mu}\mathbf{B}(\mathbf{r})|$. In practice, the magnetic trap is compressed until the bias amounts to only a few Gauss. This means that fluctuations should be very small which is not trivial because the bias results from the subtraction of two large magnetic fields, the magnetic bottle field and the antibias field. For our setup this calls for a current stability superior to 10^{-4} . Furthermore, when loading the magnetic trap or releasing the atoms, we need to be able to quickly switch on and off the magnetic field, *i.e.* typically faster than within 100 μs [11]. In summary, the current control circuitry has to fulfill several demanding requirements, since we ask for high current, low noise, independent tuning of part of the current, and fast switching. The details of the current switch will be detailed elsewhere [19].

Once the geometry of the coils is known, calculating the magnetic fields $\mathbf{B}(\mathbf{r})$ is very easy. For simple geometrical shapes of the coils, one can use analytic formulae [20] containing elliptical integrals. For complicated shapes of the coils or asymmetric arrangements, we numerically integrate the Biot-Savart formula

$$\mathbf{B}(\mathbf{r}) = \frac{\mu_0 I}{4\pi} \oint_C \frac{d\mathbf{s} \times (\mathbf{r} - \mathbf{s})}{|\mathbf{r} - \mathbf{s}|^3}, \quad (1)$$

where $\mathbf{s} = \mathbf{s}(\zeta)$ is the current path parametrized in small steps ζ . From such calculations, we determine to first order the following data characterizing our cloverleaf trap close to its center. The magnetic field gradient per ampere produced by the current I_{clov} flowing through the cloverleaf coils is $\partial_r B_{\text{clov}}/I_{\text{clov}} = 0.438$ G/cm/A. The curvature of the magnetic bottle field generated by the current I_{pinch} in the pinch coils is in radial direction $\partial_r^2 B_{\text{pinch}}/I_{\text{pinch}} = -0.186$ G/cm²/A and in axial direction $\partial_z^2 B_{\text{pinch}}/I_{\text{pinch}} = 0.373$ G/cm²/A. And the magnetic field amplitude produced by the pinch and the antibias fields at the trap center are $B_{\text{pinch}}/I_{\text{pinch}} = 0.767$ G/A and $B_{\text{anti}}/I_{\text{anti}} = 2.693$ G/A. We usually work with the currents $I_{\text{clov}} = I_{\text{pinch}} = 285$ A and I_{anti} variable. Inaccuracies in the geometric shape of the coils limit the level of

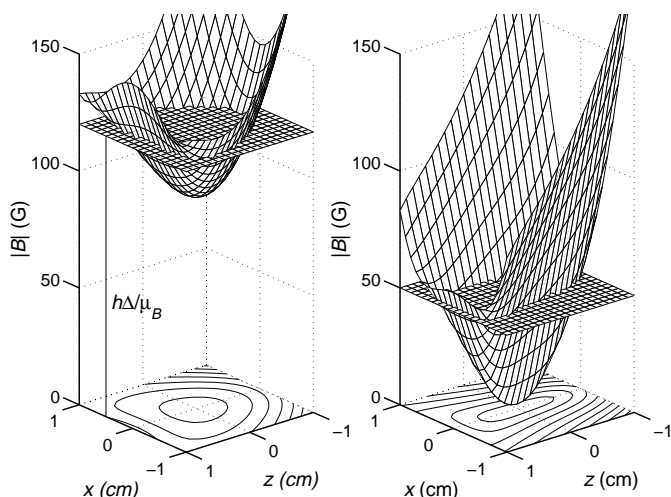


Fig. 2. Magnetic trapping potentials in the isotropic and the compressed case. The experimental parameters only differ in the amount of antibias current: $I_{\text{anti}} = 50$ A in the isotropic case and $I_{\text{anti}} = 85$ A in the compressed case. The planes slicing the potentials represent the laser being tuned to a Zeeman shifted resonance. Our MFT technique images the contour lines at these detunings (see text).

precision of the calculations to 10% uncertainty. However, as we will show later, we can calibrate the calculations using the MFT method and achieve uncertainties lower than 2%.

The absolute value of the magnetic fields $|\mathbf{B}(\mathbf{r})|$ is shown in Figure 2 for two different values of the antibias current. For low antibias current (left side), $I_{\text{anti}} = 50$ A, the trap is roughly isotropic at the center, the mean curvature of the magnetic field is small, and there is a large magnetic field offset, $B(0) = 100$ G. However, when we apply a high antibias current, $I_{\text{anti}} = 85$ A, the trap is axially elongated, radially compressed, and the magnetic field offset is small, $B(0) = 1$ G.

3 Magnetic field tomography

The basic idea of magnetic field tomography can be subsumed as “laser excitation spectroscopy on Zeeman-shifted electronic transitions with spatially resolved fluorescence detection”. We are detailing this idea in the following. The Hamiltonian of atoms with the electron total angular momentum $\boldsymbol{\mu}_J = g_J \mu_B \mathbf{J}$ and the nuclear spin $\boldsymbol{\mu}_I = g_I \mu_N \mathbf{I}$ subject to a magnetic field \mathbf{B} reads [21]

$$H_{\text{hfs}} + H_B = A_J \mathbf{I} \mathbf{J} + B_J \frac{6(\mathbf{I} \mathbf{J})^2 + 3\mathbf{I} \mathbf{J} - 2I(I+1)J(J+1)}{2I(2I-1)2J(2J-1)} - \boldsymbol{\mu}_J \mathbf{B} - \boldsymbol{\mu}_I \mathbf{B}. \quad (2)$$

The first term corresponds to the magnetic dipole interaction, and A_J is called the *hyperfine constant*. For sodium it takes the values $A_J(3^2S_{1/2}) = 885.8$ MHz

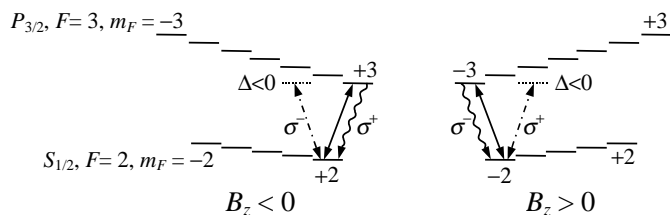


Fig. 3. Level scheme of the sodium $D2$ -line between the hyperfine levels $F = 2$ and $F' = 3$.

and $A_J(3^2P_{3/2}) = 18.65$ MHz [21]. The second term corresponds to the electrostatic interaction of the nuclear quadrupole moment. The *constant of the quadrupole interaction* for sodium, $B_J(3^2P_{3/2}) = 2.82$ MHz, is small but not negligible. The next two terms describe the interaction of the atom with the external magnetic field. The contribution containing the nuclear magneton μ_N is negligibly small. It is interesting to point out the behavior of the *fully stretched* spin states $|F = J + I, m_F = \pm F\rangle$. For those states the shift due to the interaction (2) is linear in $|\mathbf{B}|$. The shifts of all other states, since our magnetic trap operates in an intermediate regime of magnetic fields where the hyperfine coupling is perturbed by the magnetic fields, are conveniently numerically calculated as the eigenvalues of the Hamiltonian. In order to keep the analysis simple, we will first concentrate on the fully stretched states. However, we will need to stress the full expression to describe several features of our observations.

When a laser is irradiated on an electronic transition with Zeeman degeneracy, the situation gets more complicated, because the Zeeman substates can be coupled by the laser, optical pumping takes place, and the energy levels are additionally shifted by the dynamical Stark-effect by an amount that depends on the Rabi frequency $\Omega = \mathbf{d} \cdot \mathbf{E}/\hbar$, where \mathbf{d} denotes the electric dipole moment of the transition, and \mathbf{E} denotes the electrical field amplitude of the light. We will focus here on an approximation that holds in our experiment, *i.e.* the Rabi frequency is weak compared to the Larmor frequency $\omega_L = \boldsymbol{\mu} \mathbf{B}/\hbar$. Then the energy levels are mainly shifted by the Zeeman-effect, and we may disregard the light shift. In this case, the magnetic field direction lends itself naturally as the quantization axis, because the Hamiltonian is diagonal with respect to this axis.

For a laser irradiated on an electronic resonance to induce transitions, these transitions must be allowed by selection rules. Electric dipole transitions *e.g.* require $F' - F = 0, \pm 1$ and $m_{F'} - m_F = 0, \pm 1$, where the prime denotes the excited level. In an external magnetic field these transitions are not degenerate, so that magnetic field probing *via* observation of the fluorescence as a function of laser detuning is not unambiguous. If we choose our atomic transition so that the total angular momentum of the upper level is superior by 1 to that of the lower level, $F' = F + 1$, and if we apply a particular laser polarization, *i.e.* σ^+ or σ^- respectively, we drive a so-called *cycling transition*, *i.e.* the excited state can only decay into the very same ground state (see Fig. 3). The cycling

transition involves the levels $S_{1/2}$, $F = 2$, $m_F = \pm 2$ and $P_{3/2}$, $F' = 3$, $m_{F'} = \pm 3$. Assume for example a laser beam irradiated along the z -axis, $\mathbf{k} = k\hat{\mathbf{e}}_z$, inside a magnetic field oriented in the same direction, $\mathbf{B} = B_z\hat{\mathbf{e}}_z$. The choice of the z -axis defines the labelling of the light polarization, *i.e.* the light polarization called σ^- is the one that excites transitions with $m_{F'} - m_F = -1$. Let us consider a σ^- polarized red-detuned laser $\Delta < 0$. For atoms subject to a positive magnetic field, $B_z > 0$ the laser then drives the cycling transition $m_F = F = 2$ and $m_{F'} = F' = 3$, while atoms that are subject to negative $B_z < 0$ are off resonance. By inverting either the polarization or the detuning, we probe the atoms that are subject to negative B_z . This simple picture only holds if we can assume to have a strong magnetic offset field in z -direction, $|\mathbf{B}| \approx |B_z|$, which is the case for the field to be investigated here. We will see that the condition is less restrictive than it seems in the first place.

Because our cycling transition effectively realizes a *two-level atom*, the expression for the resonance fluorescence in terms of scattered photon numbers S per probing time t_{probe} takes a very simple form:

$$S = \frac{I}{\hbar\omega} \sigma N_{\text{at}} t_{\text{probe}}, \quad (3)$$

where I is the intensity of the irradiated light, N_{at} the number of atoms in the interaction zone, and the optical cross-section is

$$\sigma = \frac{\sigma_0 \Gamma^2}{4[\Delta - \hbar^{-1}(\boldsymbol{\mu}' - \boldsymbol{\mu})\mathbf{B}]^2 + 2\Omega^2 + \Gamma^2}, \quad (4)$$

where $\Gamma = 2\pi \times 9.89$ MHz is the natural linewidth of the sodium $D2$ line, and $\Omega = \sqrt{\sigma_0 \Gamma I / \hbar\omega}$ is the Rabi frequency. For the cycling transition between the fully stretched states we find

$$(\boldsymbol{\mu}' - \boldsymbol{\mu})\mathbf{B} = \mu_B (g_{F'} m_{F'} - g_F m_F) \varsigma |\mathbf{B}| = \pm \mu_B \varsigma |\mathbf{B}|$$

for σ^\pm polarized light, where $\varsigma = \text{sign}(B_z)$ and the Landé factors are $g_F = 1/2$ and $g_{F'} = 2/3$.

The light is scattered at a nondegenerate transition between magnetic sublevels so that we have to weight the coupling strength (*i.e.* the Rabi frequency) with the relative strength of the specific transition. The relative coupling strength can be expressed by $\{6j\}$ symbols which reflect the fine and the hyperfine structure coupling and by $\{3j\}$ symbols for the coupling of the atomic angular momenta to the magnetic field [21]. For the cycling transition of interest, the relative coupling strength is 1. In those cases where \mathbf{B} is not perfectly parallel to $\hat{\mathbf{e}}_z$, the coupling strength depends on the relative orientation of the polarization of the irradiated light and the magnetic field direction $\hat{\boldsymbol{\epsilon}}\hat{\mathbf{B}}$. Those effects can be included in our description by using a modified Rabi frequency $\Omega_{\hat{\boldsymbol{\epsilon}}\hat{\mathbf{B}}}$. However, we will see later that we do not need to specify the functional dependence for our purpose.

The above considerations hold for single atoms interacting with a magnetic and an optical field. In the following, we will address the question how these atoms can

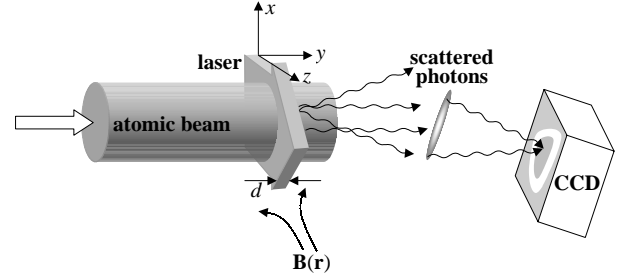


Fig. 4. Scheme of the tomographic measurement experiment with atomic beam, laser light sheet and imaging system. The symmetry axis of the cloverleaf trap is along $\hat{\mathbf{e}}_z$. The imaging system is inclined by 22.5° with respect to the atomic beam axis.

be utilized for magnetic field tomography. We consider spatially inhomogeneous fields $\mathbf{B}(\mathbf{r})$ and $\mathbf{E}(\mathbf{r})$ and specify the physical situation further by assuming that the spatial extent of the magnetic field is much larger than the interaction zone of the atoms with the light field. In fact, we will use a hot atomic beam perpendicularly intersected by a thin sheet of laser light. This allows us to disregard the impact of the magnetic field gradient on the atomic motion. We define our coordinate system by calling the propagation direction of the laser beam z -axis and the normal vector of the light sheet plane y -axis (see Fig. 4). The light sheet may be displaced along the y -axis by an amount y_0 and has an inhomogeneous Gaussian intensity distribution along the x -axis so that the intensity can be written

$$I(x, y) = 2P/\pi w_0^2 e^{-2x^2/w_0^2} \chi_{[y_0-d/2, y_0+d/2]}(y), \quad (5)$$

where $w_0 \approx 1$ cm is the beam waist and $P \approx 100$ mW the laser power. The laser light has a well-defined polarization σ^\pm or π . The atomic beam is assumed to provide a homogeneous atomic density in the interaction region $n(\mathbf{r}) \approx n_0 \approx 9 \times 10^6$ cm $^{-3}$.

The fluorescence is collected along the y -axis, *i.e.* we integrate the fluorescence signal across the thin slice. A lens system images the scattered light so that we obtain a spatially modulated photon flux which can be expressed through a generalization of equation (3) by

$$S_{\Delta, y_0, \varsigma}(x, z) = \alpha t_{\text{probe}} \int_{-d/2}^{d/2} \frac{I(x, y)}{\hbar\omega} n(\mathbf{r}) \sigma(\mathbf{r}, \Delta) dy \\ \approx \frac{\alpha t_{\text{probe}} n_0 d \Gamma \Omega_{\hat{\boldsymbol{\epsilon}}\hat{\mathbf{B}}}(x, y_0, z)^2}{4[\Delta - \hbar^{-1} \varsigma \mu_B |\mathbf{B}(x, y_0, z)|]^2 + 2\Omega_{\hat{\boldsymbol{\epsilon}}\hat{\mathbf{B}}}(x, y_0, z)^2 + \Gamma^2}. \quad (6)$$

The z dependence of the Rabi frequency comes from the dependence of the coupling strength on the relative orientation of $\hat{\boldsymbol{\epsilon}}$ and \mathbf{B} . The photon flux arriving at the image plane is recorded with a CCD camera. The proportionality constant α can be estimated knowing the camera pixel size $d_{\text{pxl}} = 9$ μm , its sensitivity (including quantum efficiency and electronic gain) $\eta_{\text{CCD}} = 1$ count/100 photons,

the light collection solid angle of the imaging lens system $\Omega_{\text{sa}} = 0.06\%$, and its magnification $\zeta_{\text{mag}} = 0.17$,

$$\alpha = \frac{d_{\text{pxl}}^2}{2\zeta_{\text{mag}}} \eta_{\text{CCD}} \Omega_{\text{sa}}. \quad (7)$$

We typically integrate the signal for $t_{\text{probe}} = 500$ ms.

Equation (6) immediately reveals that, because we assumed strong magnetic fields, the fluorescence nearly vanishes everywhere where the resonance condition $\Delta = \pm \hbar^{-1} \mu_B |\mathbf{B}(\mathbf{r})|$ is not satisfied, or in other words, the laser light slices the magnetic field at a given field strength $|\mathbf{B}(\mathbf{r})| = \mp \hbar \Delta / \mu_B$. The spatial distribution of the fluorescence reflects the *modulus* of the magnetic field. This situation is depicted in Figure 2 by a plane that interpenetrates the magnetic potential. For a given detuning Δ , light sheet position y_0 , and polarization λ we expect the fluorescence image $S_{\Delta, y_0, \varsigma}(x, z)$ to form a narrow ridge along a closed path which basically traces a two-dimensional equipotential contour line of the magnetic field constrained to the plane of the laser light sheet (see Fig. 5). At the top of the fluorescence ridge the photon count rate reads

$$S_{\Delta, y_0, \varsigma}(x, z) \approx \alpha t_{\text{probe}} \frac{n_0 d \Gamma \Omega_{\hat{\epsilon} \hat{\mathbf{B}}}(x, y_0, z)^2}{2 \Omega_{\hat{\epsilon} \hat{\mathbf{B}}}(x, y_0, z)^2 + \Gamma^2}, \quad (8)$$

where $\hbar \Delta = \varsigma \mu_B B(\mathbf{r})$. We see that the location of the ridge is not influenced by the dependence of the Rabi frequency on $\hat{\epsilon} \hat{\mathbf{B}}$, but the height of the ridge is modulated. Furthermore, the contrast of this modulation vanishes as saturation is approached, $\Omega \rightarrow \Gamma$. Another reason for a modulated fluorescence is the imperfect homogeneity of the atomic density $n(\mathbf{r})$. This contribution, however, is easily avoided by normalizing the fluorescence image with an image at zero magnetic field.

As we stated earlier, the cloverleaf trap is, in axial direction, a magnetic bottle, *i.e.* the trapping potential is situated on top of a large magnetic field offset pointing in z -direction. In this case, $B_z/|\mathbf{B}| \approx +1$, and we get the whole equipotential line using a single σ^+ (or σ^-) laser polarization. However, this does not hold true for very compressed traps when the field offset is compensated by a homogeneous antibias field. Then in some regions of space, we may have $B_z/|\mathbf{B}| < 0$. For the same reason, quadrupolar fields (or more generally, fields which are antisymmetric with respect to the z -axis) are only half imaged with a single circularly polarized laser. However, if we irradiate linearly polarized light, which is a linear superposition of left and right circularly polarized light, we get the complete image $\sum_{\varsigma=\pm 1} S_{\Delta, y_0, \varsigma}(x, z)$.

4 The experiment

In our experiment, we use a fast atomic beam to probe the magnetic field. Hot sodium atoms are ejected from a heated oven through a fine nozzle. After a 2 m long distance, they arrive at the interaction region as a 2 cm wide highly collimated and homogeneous beam: we verified that

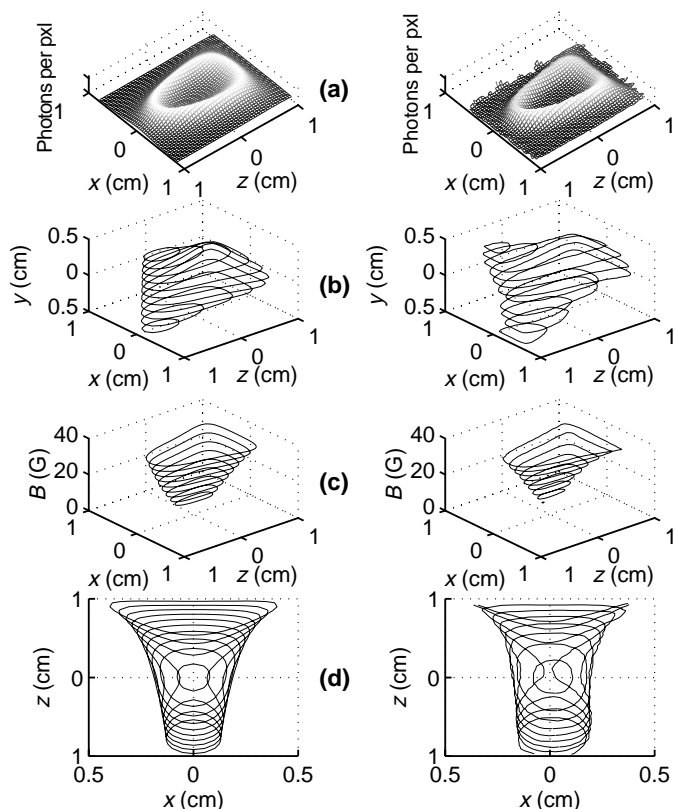


Fig. 5. (a) Calculated and measured fluorescence image of a light scattering atomic beam inside a cloverleaf-shaped magnetic field with $I_{\text{clov}} = 285$ A and $I_{\text{anti}} = 80$ A. The laser is linearly polarized and detuned +50 MHz from resonance. (b–d) Equipotential lines derived from fluorescence images as shown in (a). In (b) the antibias current is $I_{\text{anti}} = 85$ A, the detuning is +64 MHz, and the light is σ^- polarized. The different lines correspond to different locations of the laser slice displaced from one another by 1 mm. In (c) the slice is kept at the center, the antibias current at $I_{\text{anti}} = 80$ A, and the detuning is ramped from +10 MHz to +50 MHz. In (d) the slice is in the center, the detuning is fixed at +25 MHz, and the antibias current is ramped from $I_{\text{anti}} = 80$ A to $I_{\text{anti}} = 100$ A.

the radial velocity distribution v_{\perp} is narrow enough to allow us to neglect the transversal Doppler effect at the $D2$ atomic resonance, $kv_{\perp} < \Gamma$. The atoms enter the magnetic field with a velocity satisfying $\partial_t B/B \ll \Omega_L$ which allows the assumption that the atomic spin adiabatically follows the fields.

In the interaction region the atoms cross a beam of near-resonant laser light. When magnetic fields are present, the fluorescence scattering is spatially modulated by the inhomogeneous Zeeman-shift of the resonant levels. The fluorescence can conveniently be imaged to a CCD camera. Blurring of the images by column integration along the imaging direction can be avoided by only irradiating a thin sheet of light whose plane is orthogonal to the imaging axis. In this way, two spatial dimensions of the magnetic field are directly imaged and the third is probed by moving the light sheet back and forth.

The strength of the magnetic field is measured by tuning the laser light to the Zeeman-shifted resonances, thus slicing the magnetic potential at a depth that can precisely be set by the laser frequency (see Fig. 2).

Our experiment is sketched in Figure 4, and an example of a fluorescence image is shown in Figure 5a. For this image we operated our cloverleaf trap at full current $I_{\text{clov}} = 285$ A, applied $I_a = 80$ A antibias current, and located the laser light sheet at the center of the trap. The ring-shaped border corresponds to atoms being resonant with laser light blue-shifted by $\Delta = 2\pi \times 50$ MHz. Therefore, the magnetic field along this border line is $|\mathbf{B}(\mathbf{r})| = \hbar\Delta/\mu_B = 36$ G.

By recording images of the equipotential lines for various detunings and various positions of the laser light slices along the imaging axis, we are able to reconstruct the magnetic field in three dimensions. To demonstrate this, we record several images like the one shown in Figure 5a with varied parameters. From the fluorescence maximum of every recorded image, we extract the closed ridge. For this purpose, we have written a data analyzing program which, from an arbitrary starting point, is capable of climbing the closest maximum and discerning the path to follow the ridge. We plot all ridges into a common picture. For example, the right hand side of Figure 5b shows the equipotential lines for $\Delta = 2\pi \times 64$ MHz and $I_{\text{anti}} = 85$ A at various positions of the slice, thus forming an equipotential surface, $|\mathbf{B}(\mathbf{r})| = \text{const}$. If we know the surfaces for all values of const , we can reconstruct the three-dimensional magnetic vector field $\mathbf{B}(\mathbf{r})$. To record equipotential surfaces at other magnetic field strengths, we repeat the procedure for different laser detunings. This is demonstrated in Figure 5c where we kept the light sheet at the trap center and varied the detunings between 10 MHz and 50 MHz. Figure 5d shows the equipotential lines for fixed detuning of $\Delta = 2\pi \times 25$ MHz and centered light sheet position but varied antibias current.

The left hand sides of the Figures 5a–5d show the result of calculations using formula (1). In order to improve the calculations, we calibrated them by measurements using a procedure to be detailed in the following paragraph. The remaining small discrepancies between theory and experiment are probably due to the inhomogeneous intensity distribution within the laser beam.

When we drive the $D2$ line with σ^+ light, five transitions between the hyperfine levels $^2S_{1/2}$, $F = 2$ and $^2P_{3/2}$, $F' = 3$ satisfy the selection rule $m_{F'} - m_F = 1$. Under certain conditions, we experimentally observe all of them simultaneously, since the laser can be resonant with different transitions simultaneously at different regions of space, where the magnetic field has different values $|\mathbf{B}(\mathbf{r})| = \hbar\Delta/[\mu_B(g_{F'}m_{F'} - g_Fm_F)]$. The right hand side of Figure 6a shows such a fluorescence image. When performing the calculations (left hand side of the figure), it is essential to take into account the nonlinear dependence of the Zeeman-shift on the magnetic field for transitions between non-stretched states (Paschen-Back regime of the hyperfine structure). For calculating the curves in

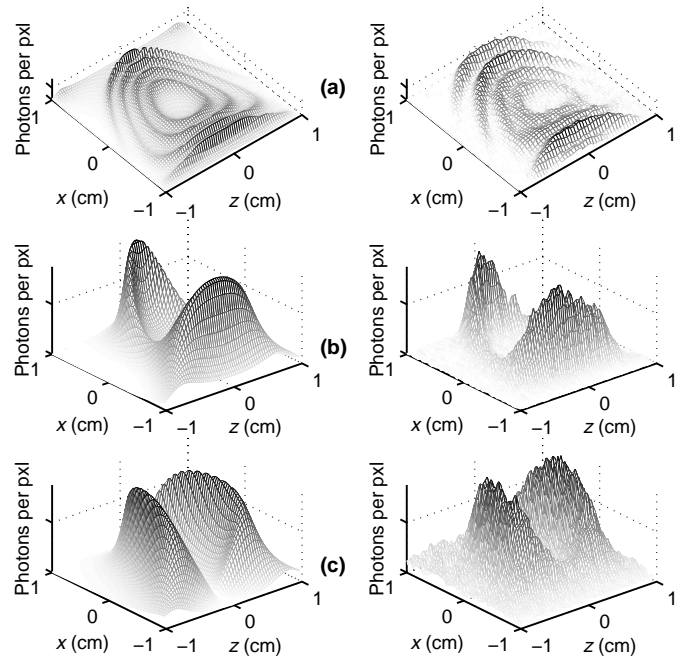


Fig. 6. (a) Multiple magnetic field tomographic lines. When the dynamic range of the magnetic field strength is large enough, we observe the Zeeman splitting of the σ^+ transitions as multiple tomographic lines. The figures correspond to the cloverleaf trap parameters $I_{\text{clov}} = 285$ A and $I_{\text{anti}} = 60$ A, and the detuning is +20 MHz. The four ridges correspond from the inside to the outside to the transitions $(m_F, m_F') = (2, 3)$, $(1, 2)$, $(0, 1)$, and $(-1, 0)$. The noise in the measured data has been reduced to increase the visibility of the features. (b) and (c) The fluorescence light is polarized, and the polarization depends on the local magnetic field. In (b) it has been filtered with a polarizer oriented to transmit light being linearly polarized along $\hat{\epsilon} = \hat{e}_z$. In (c) $\hat{\epsilon} = \hat{e}_x$ light is left through.

Figure 6a, we numerically diagonalize the matrix (2) for the ground and excited hyperfine level.

Furthermore, we observe that the fluorescence light is polarized and that the polarization of is spatially modulated by the magnetic field. For the images shown in Figures 6b and 6c, we filtered the fluorescence light in front of the camera with a linear polarizer. The fluorescence ridge does not move, however, its contrast is strongly modulated and changes when we set the transmitting axis of the polarizer along $\hat{\pi} = \hat{e}_z$ (Fig. 6b) or $\hat{\pi} = \hat{e}_x$ (Fig. 6c). The behavior is easily understood in terms of the radiation pattern of an atomic dipole inside a magnetic field. In all directions orthogonal to \mathbf{B} the atom emits linearly polarized σ light. In the plane which is sliced by our laser light sheet, our cloverleaf trap yields $\mathbf{B}(x, 0, z) \perp \hat{e}_y$, so that we expect linearly polarized light, indeed. And since $\mathbf{B}(x, 0, z)$ rotates along the fluorescence ridge, the polarization of the scattered light does so, as well. The left two pictures show the result of calculations according to

$$S_{\Delta, y_0, \varsigma}^{(\pi)}(x, z) = S_{\Delta, y_0, \varsigma}(x, z) \frac{|\mathbf{B}(\mathbf{r}) \times \hat{\pi}|}{|\mathbf{B}(\mathbf{r})|}. \quad (9)$$

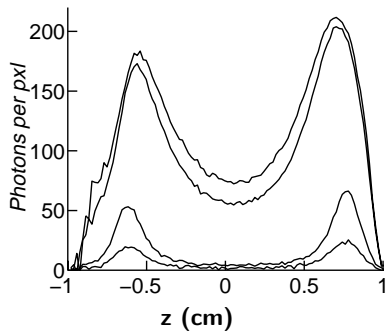


Fig. 7. Cuts through fluorescence images along a line defined by $x = y = 0$ for various laser intensities $I = 5.6, 12, 118,$ and 186 mW. The effect of power-broadening is clearly visible. The magnetic field parameters were $I_{\text{clov}} = 285$ A, $I_{\text{anti}} = 85$ A and $+40$ MHz.

The resolution of the MFT method can be defined as the halfwidth of the fluorescence ridge observed at the CCD camera. With this definition, the width $2\delta z$ of the emerging contour line in $\hat{\mathbf{e}}_z$ direction immediately follows from equation (6), $2\delta z = \hbar\sqrt{\Gamma^2 + 2\Omega_{\hat{\mathbf{e}}\mathbf{B}}^2}/(\mu_B\partial_z|\mathbf{B}|)$. Thus it depends on the magnetic field gradient and on the (power-broadened) linewidth of the $D2$ resonance. In terms of magnetic fields the resolution is given by $\delta B = \partial_z|\mathbf{B}|\delta z$, and we see that, even if we work below saturation, $\Omega \ll \Gamma$, we are not sensitive to magnetic field variations that are weaker than $\delta B \approx 3.6$ G. Figure 7 shows cuts through fluorescence images along a line defined by $x = y = 0$ for various laser intensities. The fluorescence rate increases proportionally with low laser intensities, but saturates at high intensities. The highest spatial resolution found was about 1 mm^3 at a location where the axial field gradient was $\partial_z|\mathbf{B}| \approx 50$ G/cm which corresponds to $\delta B \approx 5$ G. We could, in principle, use narrower (Raman) transitions. However, the fluorescence rate will be lowered as well, thus requiring a more sensitive detection system.

The MFT method can also be used to precisely determine the amount of antibias current necessary for exact compensation of the offset field created by the pinch coils. For this purpose, we set the antibias current to some value I_{anti} , observe the fluorescence distribution (Fig. 5a) on-line, and find the laser detuning Δ at which the fluorescence disappears. This gives us the minimum of B_z . We repeat this procedure for various antibias currents and obtain two curves, one for σ^- and one for σ^+ polarized light. The curves intersect near $\Delta = 0$. At this detuning the antibias is perfectly compensated, *i.e.* the magnetic trap has maximum compression. The curves are shown in Figure 8. The compensation current is $I_{\text{anti}} = (86.1 \pm 1.1)$ A. As we see, the uncertainty of this method is rather small. Furthermore, the slopes of the curves in Figure 8 yield the calibration of the pinch coils, $B_{\text{pnch}}/I_{\text{clov}} = 0.830$ G/A, and of the antibias coils, $B_{\text{anti}}/I_{\text{anti}} = 2.743$ G/A, at the center of the trap. We can now utilize these data to correct our magnetic field calculations based on formula (1). We also calibrated the current I_{clov} using the same method

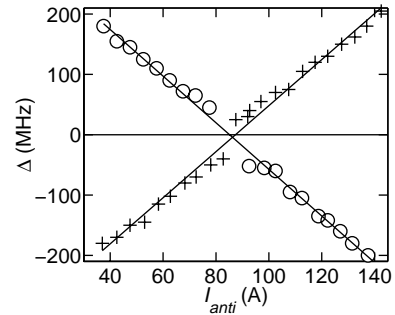


Fig. 8. Compensation of the magnetic field offset *via* I_{anti} using $I_{\text{clov}} = 285$ A. Shown is the detuning at which atoms at the bottom of the potential scatter light. These data can be used to calibrate the calculations of the magnetic fields.

and obtained values for the cloverleaf trap parameters that agree well with the above ones.

5 Conclusion

In conclusion, magnetic fields have been probed using a technique well-suited for fast three-dimensional tomographic reconstruction of a magnetic field within a volume which is not accessible to material detectors like Hall probes, *e.g.* within an ultra-high vacuum. The drawback of this method is that the resolution is obviously limited by the natural linewidth of the transition, so that it is only applicable for large magnetic fields and large field gradients. A solution to this problem could be the use of radiofrequency-optical double resonance schemes [22,23].

The MFT method is well adapted to investigating magnetic trapping fields for neutral atoms. In particular, it permits precise mapping of the trap geometry and fast localisation of its minimum. The response time of the MFT method is only limited by the time required for optical pumping. Therefore the method could be extended for monitoring rapid changes in the magnetic field strength being as fast as a few 10 ns using stroboscopic imaging or even for real-time control of the magnetic trap configuration. We conclude that, since this technique only requires a hot atomic beam and a weak tunable laser beam, we believe it to be a simple and versatile diagnostic instrument for probing magnetic fields.

We acknowledge financial support from the São Paulo State Research Foundation FAPESP and Ph.W.C. wishes to thank the Deutscher Akademischer Austauschdienst DAAD for financial support. R.K. also acknowledges support from the Centre National de la Recherche Scientifique CNRS.

References

1. E.L. Raab, M. Prentiss, A. Cable, S. Chu, D. Pritchard, *Phys. Rev. Lett.* **59**, 2631 (1987).
2. K.E. Gibble, S. Kasapi, S. Chu, *Opt. Lett.* **10**, 526 (1992).

3. T. Walker, D. Sesko, C.E. Wieman, Phys. Rev. Lett. **64**, 408 (1990).
4. T. Ido, Y. Isoya, H. Katori, Phys. Rev. A **61**, 061403(R) (2000).
5. S. Chu, J.E. Bjorkholm, A. Ashkin, A. Cable, Phys. Rev. Lett. **57**, 314 (1986).
6. D.-J. Han, S. Wolf, S. Oliver, C. McCormick, M.T. DePue, D.S. Weiss, Phys. Rev. Lett. **85**, 724 (2000).
7. W. Petrich, M.H. Anderson, J.R. Ensher, E.A. Cornell, Phys. Rev. Lett. **74**, 3352 (1995).
8. D.E. Pritchard, Phys. Rev. Lett. **51**, 1336 (1983).
9. M.O. Mewes, M.R. Andrews, N.J. van Druten, D.M. Kurn, D.S. Durfee, W. Ketterle, Phys. Rev. Lett. **77**, 416 (1996).
10. H. Hess, Phys. Rev. B **34**, 3476 (1986).
11. M.H. Anderson, J.R. Ensher, M.R. Matthews, C.E. Wieman, E.A. Cornell, Science **269**, 198 (1995).
12. C.R. Monroe, E.A. Cornell, C.A. Sackett, C.J. Myatt, C.E. Wieman, Phys. Rev. Lett. **70**, 414 (1993).
13. W. Ketterle, D.S. Durfee, D.M. Stamper-Kurn, Proc. Int. School of Phys. "Enrico Fermi" **CXL**, 67 (1999).
14. W.G. Kaenders, F. Lison, I. Müller, A. Richter, R. Wynands, D. Meschede, Phys. Rev. A **54**, 5067 (1996).
15. J.J. Tolett, C.C. Bradley, C.A. Sackett, R.G. Hulet, Phys. Rev. A **51**, R22 (1995).
16. B. Desruelle, V. Boyer, P. Bouyer, G. Birkl, M. Lécrivain, F. Alves, C.I. Westbrook, A. Aspect, Eur. Phys. J. D **1**, 255 (1998).
17. T.W. Hänsch, I. Bloch, T. Esslinger, Phys. Rev. Lett. **82**, 3008 (1999).
18. W. Ketterle, N.J. van Druten, At. Mol. Opt. Phys. **37**, 181 (1996).
19. S.R. Muniz, E. Mosman, Ph.W. Courteille, K. Magalhães, L.G. Marcassa, V.S. Bagnato (unpublished).
20. T. Bergeman, Phys. Rev. A **35**, 1535 (1987).
21. H.J. Metcalf, P. van der Straten, *Laser Cooling and Trapping* (Springer-Verlag, New York, 1999).
22. A.G. Martin, K. Helmerson, V.S. Bagnato, G.P. Lafyatis, D.E. Pritchard, Phys. Rev. Lett. **61**, 2431 (1988).
23. K. Helmerson, A. Martin, D.E. Pritchard, J. Opt. Soc. Am. **9**, 483 (1992).